Int. J. Electrochem. Sci., 15 **(2020)** 5115 – 5132, doi: 10.20964/2020.06.14

International Journal of
ELECTROCHEMICAL
SCIENCE
www.electrochemsci.org

Research on Transient Model in Porous Electrode of Zn-Ni Single Flow Battery Based on REV Scale

Shouguang Yao[*], *Qiankun Jin*[*], *Zeyi Sun*, *Yi Ji*

Jiangsu University of Science and Technology,Zhengjiang212003,China
[*]E-mail: zjyaosg@126.com, qkjinedu@163.com

Received: 3 February 2020 / *Accepted:* 30 March 2020 / *Published:* 10 May 2020

To obtain the variation law of OH^- ion concentration and its influencing factors in the porous electrode of a zinc-nickel single-flow battery during battery charging, the lattice Boltzmann method is used in this study to simulate the transient mass transfer and electrochemical reaction via the (voxel)REV scale. The output is compared with pore scale. Results prove that the REV and the pore scale are consistent in the concentration distribution of the entire OH^- field.The general law of the electrochemical reaction mechanism inside the porous electrode can be obtained by increasing current density,thus reducing charging time. However, the effect of reducing the charging time gradually decreases as the current density increases, and excessive current density causes considerable concentration polarization.When the electrode thickness is too large, the diffusion resistance of OH^--ions increases. When the thickness of the electrode is too large,and the porosity of the porous electrode is too small, the diffusion resistance of OH^--ions increases. This occurrence is not conducive to the diffusion of OH^--ions. Both cause large concentration polarization in the electrode.

Keywords: Lattice Boltzmann Method（LBM）, REV scale, porous medium seepage, zinc-nickel single-flow battery, transient model

1. INTRODUCTION

The environmental pollution and energy problems caused by conventional fossil energy are becoming increasingly prominent, New energy technology, such as wind and solar energy is being developed heavily. Large-scale energy storage technology must be developed to achieve stable power supply in new energy technology.[1-3] Flow battery is a new type of energy storage and highly efficient conversion device, and it is widely used because of its high storage efficiency, excellent performance, safety ,reliability, and flexible handling. Zinc-nickel single-flow battery is a new type of single-deposition flow battery system proposed after comprehensive analysis of the advantages and disadvantages of traditional zinc-nickel batteries and the characteristics of single-flow lead-acid batteries.

[4,5]Density, simple structure and low cost are attracting increasing attention in recent years. Substantial basic research is performed on battery structure, electrolyte properties, operating conditions, and side reactions of zinc–nickel single-flow batteries [6-10]. However, to further improve battery power and service life,a microscale study of the complex electrochemical reaction mechanism must be conducted.The Lattice Boltzmann Method (LBM), as a numerical method for micro-scale research, widely used in battery micro-scale research. The simulation of porous media seepage mainly involves pore scale and (characteristic voxel) REV scale. LBM at the REV scale takes a control body as the research object to solve the REV volume average macroscopic flow volume, The fluid and medium are described by appropriate processing methods. In previous studies, scholars analyzed and simulated porous media using LBM at the REV. Liao[11] used a REV-scale dual distribution function model to simulate the biological reaction process in a porous medium in a biofuel cell to obtain the concentration and flow fields of hydrogen and glucose solutions. Xu[12] established a REV model for analyzing the electrochemical performance of porous electrodes in solid oxide fuel cells, and studied the structure, operating temperature, and fuel composition of porous electrodes on the voltammetric characteristics as well as the concentration polarization of solid oxide fuel cells influence. Zhao[13] proposed a lattice Boltzmann (LB) model based on the REV scale to simulate gas transport in a 2D microporous medium reconstructed by an optimized four-parameter random growth (QSGS) method. The velocity distribution and apparent permeability of gas transport in reconstructed porous media were demonstrated and analyzed. Liu[14] carried out the REV scale simulation of micro-fractured unconventional gas reservoirs. Based on the REV scale LB method model, and gas transport mechanism, a new REV unconventional gas flow simulation model was proposed to simulate the gas transport effect of mechanism on matrix permeability and effective permeability. Previous reports show that scholars used the REV-scale LBM method to simulate the flow, mass transfer, and chemical reactions in a medium with a porous structure. However, in fuel cells and shale gas, gases are mainly used for transmission or reaction. Zinc-nickel single-flow battery is different. Electrolyte fluid is the main reaction medium, which makes internal mass transfer and electrochemical reaction process different from the above reports.

For zinc-nickel single-fluid batteries, the effects of electrolyte flow rate, charge-discharge current, and flow channel type on battery performance during charging and discharging reported from a macro perspective. Among them, Xiao[15] recently established a 3D steady-state model of the internal reaction and mass transfer of a zinc-nickel single-flow battery, studied the ion concentration and current density distribution inside the battery, and provided an external characteristic model that depends on internal reaction parameters. basis. Based on a comprehensive description of mass, momentum, and charge transport and conservation, combined with global kinetic models involving ionic and proton reactions, Yao[16] further established a two-dimensional transient model of a zinc-nickel single-flow battery, The effects of concentration, flow rate, and charge current density changes were verified and studied experimentally. However, the use of LBM to analyze the micro-scale electrochemical reaction mechanism inside the zinc-nickel single-flow battery electrodes is limited. Yao[17, 18] established a 2D numerical pore analysis model based on the pore scale to simulate the effects of electrolyte inlet flow rate, current density, and porosity on the mass transfer and electrochemical reactions in the porous electrode of the battery under steady state conditions. Subsequently, based on the REV-scale LBM method, the reaction mechanism of the porous positive electrode of a zinc-nickel single-flow battery

under steady-state conditions was studied [19]. Existing research failed to analyze the micro-scale electrochemical reaction mechanism inside zinc-nickel single-flow battery electrodes at the REV scale using transient analysis models. The current work intends to use the LBM method of the REV scale to establish a transient flow mass transfer and electrochemical reaction analysis model inside a zinc-nickel single-fluid cell porous electrode and to simulate the transient flow mass transfer and electrochemical reaction inside the electrode. The effects of charging current density, electrode thickness ,and porosity on its electrochemical reactions were analyzed as well.

2. LBM CALCULATION MODEL

2.1 Battery reaction principle and basic reaction equation

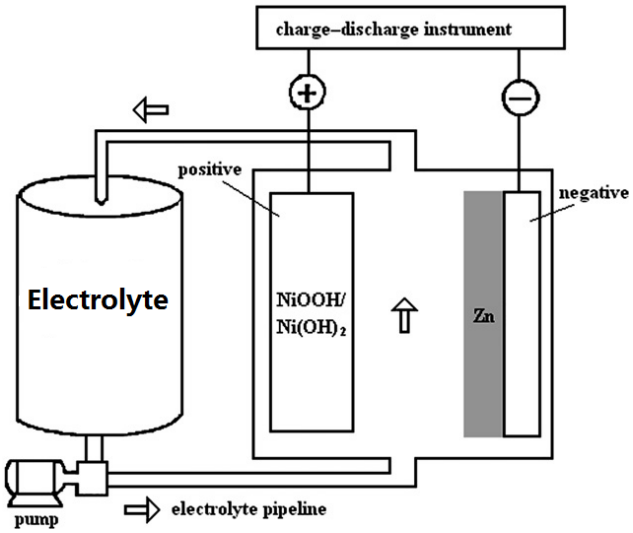

Figure 1. Basic flow chart of zinc–nickel single flow battery

Figure 1 shows that the electrolyte flows out of the tank, enters the reactor through the pump for reaction, and flows out from above to enter the storage tank when the flow battery is in operation.

(1) Description of positive electrode electrochemical reaction during charging

$$2\mathrm{Ni}(OH)_2 + 2OH^- \xrightarrow{charge} 2NiOOH + 2H_2O + 2e^- \quad (1)$$

Reaction kinetic equation:

$$j_{Ni} = i_0 \left(\frac{c^{OH^-}}{c_{ref}^{OH^-}}\right)^{a_1} \left(\frac{c^{H^+}}{c_{ref}^{H^+}}\right)^{a_1} \left(\frac{c_{max}^{H^+} - c^{H^+}}{c_{max}^{H^+} - c_{ref}^{H^+}}\right)^{(1-a_1)} \left[\exp\left(\frac{a_1 F}{RT}\eta_1\right) - \exp\left(1 - \frac{(1-a)F}{RT}\eta_1\right)\right] \quad (2)$$

Among them, i_0 is the exchange current density (A/m^2), a_1 is the anode reaction transfer coefficient, and δ_1 is the overpotential (V).

$$\delta_1 = \gamma_s - \gamma_e - E_{1,ref} \quad (3)$$

where γ_s is the solid-phase potential (V) of the interface; γ_e is the liquid-phase potential (V) of the interface, and $E_{1,ref}$ is the reference electrode potential (V), given by the following:

$$E_{1,ref} = 0.221 + 0.9448\theta^3 - 1.5874\theta^2 + 0.9158\theta \quad (4)$$

where θ is a state of charge.

(2) The continuity equation and the momentum equation are given as follows:

$$\frac{\partial \rho}{\partial t} + \nabla(\rho\vec{u}) = 0 \quad (5)$$

$$\nabla[\mu(\nabla\vec{u}) + (\nabla\vec{u})^T] - \nabla P = \rho(\vec{u}\nabla)\vec{u} \quad (6)$$

(3) Transport equation of OH^-

The transport of OH^- is affected by solution flow, concentration difference, and electric field. The transportation process is described as follows:

$$\mathrm{V} = V_C + V_s + V_e \quad (7)$$

where V_c is the convection rate; V_s is the diffusion rate and V_e is the electromigration rate;The units are both $mol/m^2 \cdot s$, The expressions are given by equations (8) to (10).

$$V_c = c^{OH^-}\vec{u} \quad (8)$$

$$-V_s = D^{OH^-}\nabla c^{OH^-} \quad (9)$$

$$V_e = -\frac{zF}{RT}D^{OH^-}c^{OH^-}\nabla\varphi \quad (10)$$

where c^{OH^-} is the concentration of OH^-, φ is the potential, and D^{OH^-} is the diffusion coefficient of OH^- [20]. It is calculated by the following formula:

$$D^{OH^-} = 2.8509 \times 10^{-5} - 2.9659 \times 10^{-4}(c^{OH^-})^{0.5} + 0.013768c^{OH^-} - 0.14199(c^{OH^-})^{1.5} + 0.42661(c^{OH^-})^2 \quad (11)$$

For solid-liquid contact surfaces, the reaction source term should be added as follows:

$$\frac{\partial c^{OH^-}}{\partial t} - \nabla \cdot \left(-c^{OH^-}\vec{u} + D^{OH^-}\nabla c^{OH^-} + \frac{zF}{RT}D^{OH^-}c^{OH^-}\nabla\varphi\right) - S^{OH} = 0 \quad (12)$$

where S^{OH} is the reaction source term ($\mathrm{mol}/m^3 \cdot s$), and $S^{OH} = a_{se}j_{Ni}/F$.

2.2 Computational physical model

A small area (2000 μm × 1600 μm) is selected as the calculation area in the vertical outer surface direction of the positive electrode porous electrode surface of the battery.Figure 2 shows a simplified illustration, where B1 is the inlet of the flow channel; B2 is the entrance boundary of the porous electrode ; B3 is the collector side of the porous dielectric positive electrode and is the closed surface; and B4 and B5 are the outlets, which are set as open boundaries; The value B6 is set as a symmetrical boundary. The macro lengths of L1, L2, and L3 are 1600, 2000, and 1200 μm, respectively. In the grid model, 1600, 2000, and 1200 grids are set. The local observation area (red area in Fig. 2) is selected, and the specific ranges are X (1200 μm-1600 μm) and Y (1200 μm-1600 μm).

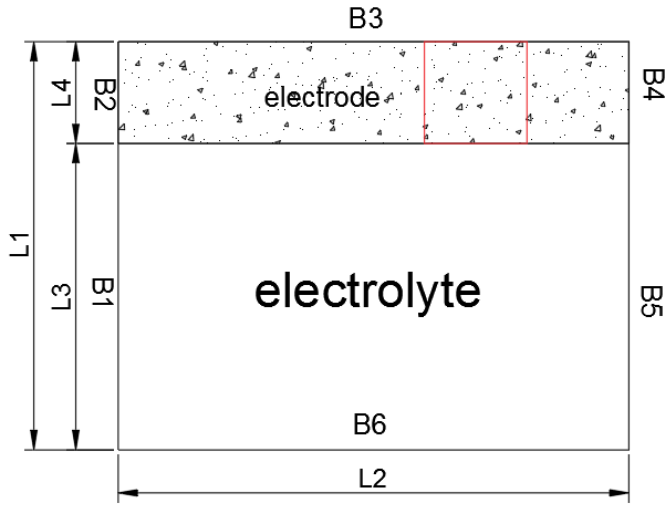

Figure 2. Computational physical model diagram

The following assumptions were made during the simulation:

(1) The temperature throughout the simulation process is unchanged;

(2) The electrolyte is laminar and considered as an incompressible fluid;

(3) The physical parameters of the electrolyte remain unchanged throughout the simulation;

(4) Battery side reactions are not considered;

(5) For the complicated electric field in the flow channel and the electrode, the electric field in the channel is assumed to be a uniform electric field to simplify the calculation. The size is determined by the electrode potential difference in the constant current charging experiment;

(6) Flow path OH^- concentration remains unchanged.

Related calculation parameters are shown in Table 1 below.

Table 1. Related calculation parameters

Parameter	Notation	Value	Unit
Reference pressure	P	0.1	MPa
Reference temperature	T	298	K
Faraday constant	F	96485	C/mol
Gas constant	R	8.314	J/mol · k
Electrode thickness	d	200,250,300,350,400	μm
Positive porosity	ε	0.35,0.45,0.55	-

Anode reaction transfer coefficient	α_1	0.5	-
OH^- concentration at the entrance	$c_{in}^{OH^-}$	8	mol/L
Electrolyte density	ρ	1.46	g/cm^3
Electrolyte viscosity	μ	3.146×10^{-3}	kg/m · s
Positive surface area	a_{se}	3864	cm^2/cm^3
Positive electrode OH^- concentration	$c_{ref}^{OH^-}$	7.1	mol/L
Positive solid particle diameter	d_p	6.0×10^{-4}	cm

2.3 Flowing LBM model

2.3.1 Generalized N-S Equation

Scholars proposed a general percolation model for the isothermal flow of incompressible fluids in porous media .This model includes not only the linear resistance (Darcy) term and the viscosity (Brinkman) term, but also the nonlinear (Forchheimer) media resistance term, which can be applied to transient seepage. The model can be expressed in the form of a generalized Navier-Stokes equation：

$$\nabla \cdot \boldsymbol{u} = 0 \quad (13)$$

$$\frac{\partial \boldsymbol{u}}{\partial t} + (\boldsymbol{u} \cdot \nabla)\left(\frac{\boldsymbol{u}}{\varepsilon}\right) = -\frac{1}{\rho}\nabla(\varepsilon p) + v_e \nabla^2 \boldsymbol{u} + \boldsymbol{F} \quad (14)$$

where ρ is the density of the fluid, u and p are the apparent velocity and pressure, $v_e = \mu_e/\rho$ is the effective kinematic viscosity coefficient, and $\boldsymbol{F}$ is the total force including the resistance of the medium and the external force. which is as follows:

$$\boldsymbol{F} = -\frac{\varepsilon v}{K}\boldsymbol{u} - \frac{\varepsilon F_\varepsilon}{\sqrt{K}}|\boldsymbol{u}|\boldsymbol{u} + \varepsilon \boldsymbol{G} \quad (15)$$

where v is the viscosity coefficient of the fluid and $\boldsymbol{G}$ is the external volume force. The structure function F_ε and permeability K are related to the porosity ε. The nickel oxide electrode in this study is a porous medium. For porous media composed of solid particles, given by Ergun's empirical correlation:

$$F_\varepsilon = \frac{1.75}{\sqrt{K\varepsilon^3}}, \quad K = \frac{\varepsilon^3 d_p^2}{150(1-\varepsilon)^2} \quad (16)$$

where d_p is the diameter of the solid particles. When no porous medium ($\varepsilon \to 1$) exists, the generalized Navier − Stokes equation (14) degenerates into the standard Navier − Stokes equation. The second term at the right end of equation (14) is the Brinkman viscosity term that reflects the boundary effect. This term can be omitted when the percolation boundary layer is thin. However, for problems involving heat or mass transfer, this term must be included in the equation. In the total force defined by equation (15), the first and second terms at the right end are the linear (Darcy) and non-linear (Forch-Heimer) media resistances.

2.3.2 LBE model

The flow LBE model in this study uses a single relaxation (BGK) model and a D2Q9 2D model with nine discrete velocities. The evolution equation of the distribution function is as follows:

$$f_i(x+\Delta x, t+\Delta t) - f_i(x,t) = -\omega\left[f_i(x,t) - f_i^{eq}(x,t)\right] + \delta_t F_i \quad (17)$$

where f_i is the particle distribution function with velocity in the i direction at x at time t, Δt is the time step;and ω represents the relaxation frequency, and

$$\omega = \frac{\Delta t}{\tau} \quad (18)$$

The relationship between fluid viscosity v and relaxation factor ω is as follows

$$v = \frac{\Delta x^2}{3\Delta t}(\omega - 0.5) \quad (19)$$

where Δx is the length of the grid, $\Delta x = c_i \Delta t$;and c_i is the discrete velocity. Using the D2Q9 model, the equilibrium distribution function f_i^{eq} and the force term F_i are:

$$f_i^{eq} = w_i \rho \left[1 + \frac{\boldsymbol{c_i \cdot u}}{c_s^2} + \frac{\boldsymbol{uu}:(c_i c_i - c_s^2 \boldsymbol{I})}{2\varepsilon c_s^4}\right] \quad (20)$$

$$F_i = \omega_i \rho \left(1 - \frac{1}{2\tau}\right)\left[\frac{c_i \cdot \boldsymbol{F}}{c_s^2} + \frac{\boldsymbol{uF}:(c_i c_i - c_s^2 \boldsymbol{I})}{\varepsilon c_s^4}\right] \quad (21)$$

Where ρ is the fluid density （kg/m^3）; the relationship between c_s and c_k is as follows

$$c_s = \frac{c_k}{\sqrt{3}} \quad (22)$$

and

$$c_k = \frac{\Delta x}{\Delta t}\vec{i} + \frac{\Delta y}{\Delta t}\vec{j} \quad (23)$$

where ω_i is the weighting factor, given by the following:

$$w_i \begin{cases} 4/9, i = 0 \\ 1/9, i = 1 \sim 4 \\ 1/36, i = 5 \sim 8 \end{cases} \quad (24)$$

The migration direction and weight factor are shown in Fig. 3:

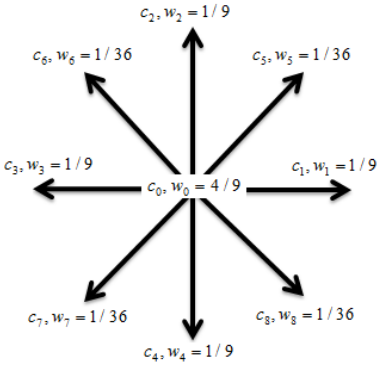

Figure 3. Schematic of migration direction and weight factor

$\boldsymbol{F}$ is given by equation (15). The equilibrium distribution function and the force term of the model include porosity ε, and the seepage density and velocity are defined as follows:

$$\rho = \sum_i f_i \ , \rho \boldsymbol{u} = \sum_i c_i f_i + \frac{\delta_t}{2}\rho \boldsymbol{F} \quad (25)$$

The value $\boldsymbol{F}$ is related to the flow velocity $\boldsymbol{u}$. Therefore, equation (29) is a quadratic nonlinear equation of velocity $\boldsymbol{u}$, The following equation can be directly derived:

$$\boldsymbol{u} = \frac{\boldsymbol{v}}{c_0 + \sqrt{c_0^2 + c_1|\boldsymbol{v}|}} \tag{26}$$

The temporary speed is as follows:

$$\rho \boldsymbol{v} = \sum_i e_i f_i + \frac{\delta_t}{2} \varepsilon \rho \boldsymbol{G} \tag{27}$$

The parameters c_0 and c_1 are the following:

$$c_0 = \frac{1}{2}\left(1 + \varepsilon \frac{\delta_t}{2} \frac{v}{K}\right), c_1 = \varepsilon \frac{\delta_t}{2} \frac{F_\varepsilon}{\sqrt{K}} \tag{28}$$

Chapman-Enskog analysis of LBE (17) shows that the corresponding macro equation is as follows:

$$\frac{\partial \rho}{\partial t} + \nabla \cdot (\rho \boldsymbol{u}) = 0 \tag{29}$$

$$\frac{\partial (\rho \boldsymbol{u})}{\partial t} + \nabla \cdot \left(\frac{\rho \boldsymbol{u}\boldsymbol{u}}{\varepsilon}\right) = -\nabla(\varepsilon p) + \nabla \cdot [\rho V_e (\nabla \boldsymbol{u} + \boldsymbol{u} \nabla)] + \boldsymbol{F} \tag{30}$$

where $\mathrm{p} = \mathrm{c}_s^2 p/\varepsilon, V_e = c_s^2(\tau - 0.5)\delta_t$.

Under incompressible approximation, equations (29) and (30) are generalized Navier-Stokes equations (13) and (14). In the porous medium region, ε in its equilibrium distribution function is taken as the permeability of the medium. In the free-flow region, $\varepsilon = 1$.

2.4 Liquid OH^- mass transfer LBM model

The liquid OH^- mass transfer process uses the D_2Q_5 model, which can ensure the calculation accuracy [21,22], and the lattice BGK equation described is as follows [23]:

$$g_i(x + \Delta x, t + \Delta t) = g_i(x, t)[1 - \omega] + \omega g_i^{eq}(x, t) - w_i S \tag{31}$$

Among them:

$$D^{OH^-} = \frac{\Delta x^2}{3\Delta t}\left(\frac{1}{\omega} - \frac{1}{2}\right) \tag{32}$$

The equilibrium distribution function is shown as follows:

$$g_i^{eq} = w_i \varphi(x, t)\left[1 + \frac{c_k \cdot \vec{u}}{c_s^2}\right] \tag{33}$$

In the formula,

$$w_i = \begin{cases} 2/6, i = 0 \\ 1/6, i = 1 \sim 4' \end{cases}$$

S is a reaction source term, which has a different expression forms on the surface of the liquid and solid phases.

(1) When reacting on a solid surface

S represents the ion reaction rate. The chemical reaction rate is given in equation (2). To distinguish the charging and discharging processes, during the charging process, set the following:

$$\mathrm{S} = i_0 \left(\frac{c^{OH^-}}{c_{ref}^{OH^-}}\right)^{a_1} \left(\frac{c^{H^+}}{c_{ref}^{H^+}}\right)^{a_1} \left[\exp\left(\frac{a_1 F}{RT}\eta_1\right) - \exp\left(-\frac{(1-a_1)F}{RT}\eta_1\right)\right] a_{se}/F \tag{34}$$

Without considering the potential, set the following:

$$\mathrm{S} = \mathrm{K}\left(\frac{c^{OH^-}}{c_{ref}^{OH^-}}\right)^{a_1} \left(\frac{c^{H^+}}{c_{ref}^{H^+}}\right)^{a_1} \tag{35}$$

During the constant current charging process, for the entire porous electrode area,

$$\frac{i}{F} = \sum S \quad (36)$$

where i is the charging current density (mA/cm^2).

(2) In the liquid phase

Ions have a certain charge. Thus, electromigration occurs during mass transfer. The governing equation of electromigration and mass transfer is as follows:

$$\mathrm{S} = \varphi(x,t) \cdot \frac{c_k}{c_s^2} \cdot \frac{zF\vec{E}}{RT} (\Delta t \Delta x^2) \quad (37)$$

Where $\vec{E}$ is the electric field.

3. RESULTS AND ANALYSIS

3.1 Comparison with pore scale

Compared with REV scale, the transient physical mass transfer process at the pore scale is basically similar to the computational physical model. The differences are mainly as follows. The calculation area of the pore scale is small, which mainly describes the mass transfer process in a single or several pores. In the simulation of the electrochemical reaction mechanism inside the porous electrode, a digital model must be established according to the structural characteristics of sintered nickel, as shown in Fig. 4.

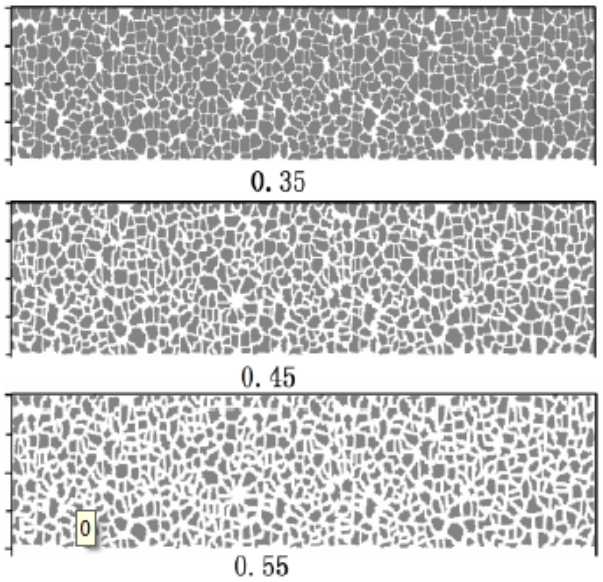

Figure 4. Numerical model of porous media

Fig. 5 (a) shows that when the current density is $12\mathrm{mA}/cm^2$ and the thickness of the positive electrode is 300 μm, under the three porosities of 0.35,0.45,0.55, changes in the average OH^- concentration in the direction of the runner and its difference in the area of porous media with the charging time step.Fig.5(b) shows the change in OH^- concentration under different porosities in the local observation area (X axis: 675–825, Y axis: 900–1200).

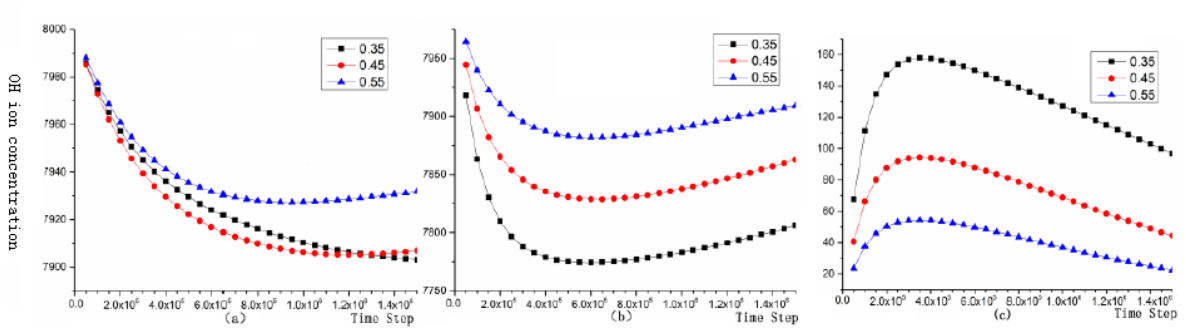

Figure 5(a). OH^- average concentration (a) Near runner side, (b) Far runner side, and (c) Difference of OH^- concentration in near and far runners

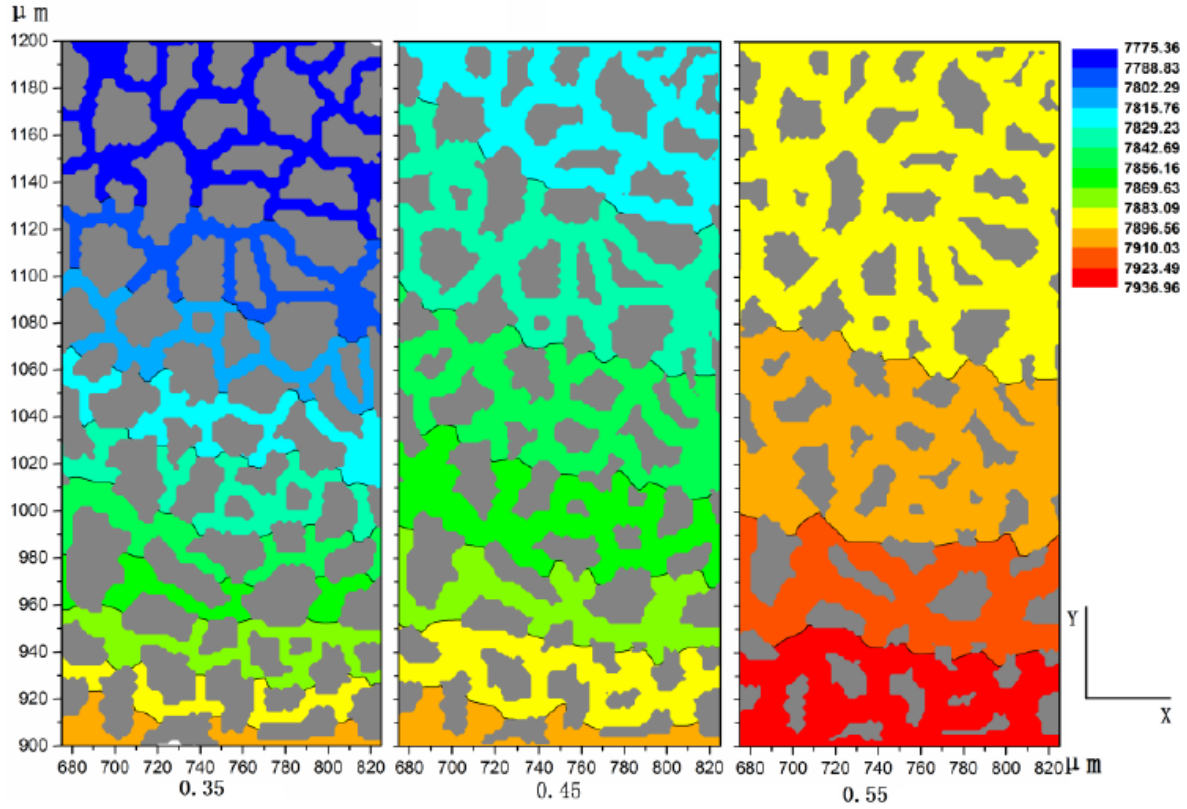

Figure 5 (b). OH^- Concentration change under different porosities

Figs. 5 (a) and 8 show the change of OH^- concentration with time step at REV scale and pore scale. Figs. 5 (b) and 9 show the change in concentration OH^- of the observation area inside the porous electrode at two scales. The calculation area of the REV scale is larger than that of the pore scale, but the variation trend of OH^- concentration with charging time is basically the same. The concentration decreases sharply at first and then slowly rises. The greater the porosity, the lower the concentration of OH^-. The OH^- on the side of the far flow channel decreases with the increase of the porosity at the beginning of charging, and then rises. The concentration difference between the two sides increases and then decreases. The greater the porosity, the greater the difference in concentration. The concentration

change of OH^- inside the porous electrode is also basically the same. The OH^- concentration on the near flow side is greater than on the far flow side. The greater the porosity, the greater the overall concentration of OH^-, but the concentration gradient of OH^- decreases [19] . Analysis shows that, compared with the pore scale, the REV scale can expand the calculation area and simulate and analyze the internal mass transfer process of the porous electrode better while ensuring simulation accuracy.

3.2 Influence of charging current density

In considering the effect of the charging current density, the electrode thickness was taken as 400 μm, and the porosity was 0.45. Figs. 6(a), (b), and (c) show that under the five current densities of $6mA/cm^2$, $9mA/cm^2$, $12mA/cm^2$, $15mA/cm^2$, $18mA/cm^2$, changes in the average OH^- concentration in the direction of the runner and its difference between the near and far runner sides in the area of porous media with the charging time step.

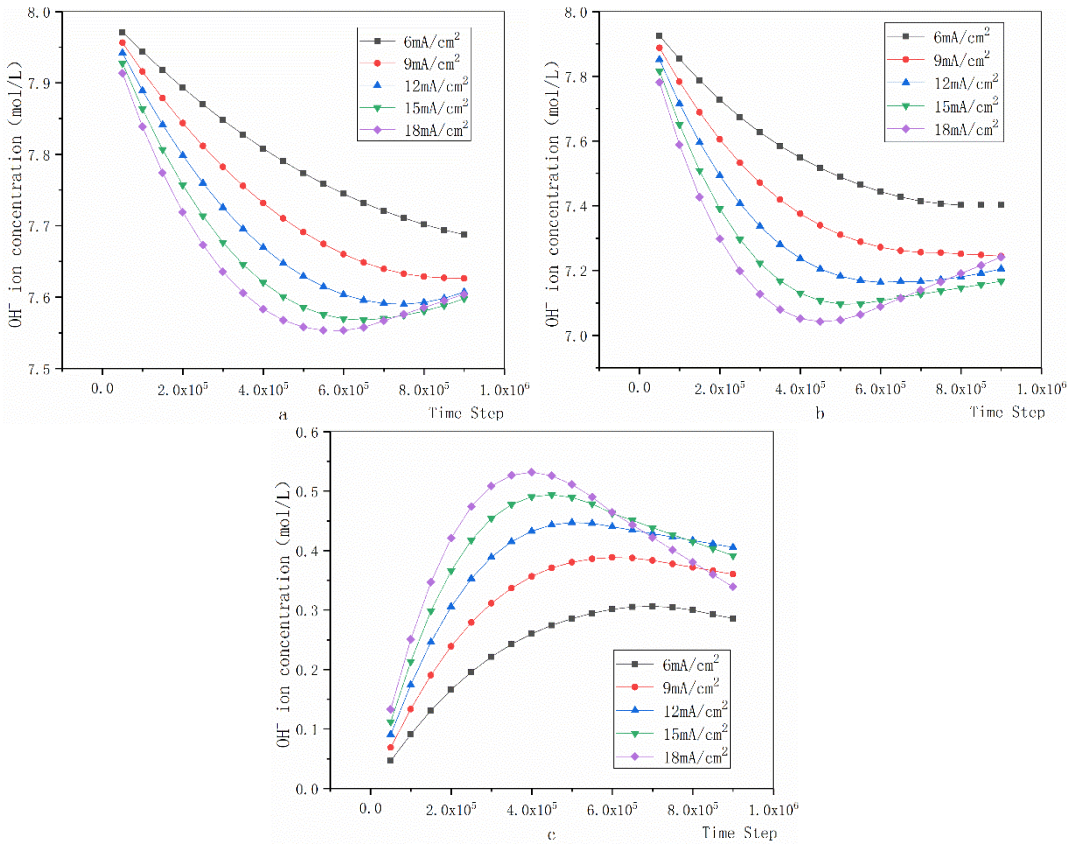

Figure 6. OH^- average concentration: (a) Near runner side, (b) Far runner side, and (c) Difference of OH^- concentration in near and far runners

Figure 6 shows that during the initial stage of charging, the average concentrations of OH^- on the near and far side of the runner gradually decrease with time step. The larger the charging current

density, the faster the decline. The difference between the average OH^- concentrations increases rapidly with time step and then decreases slowly. The greater the charging current density, the larger the maximum value. Thus, the faster the rise and fall.

Further analysis shows that an increase in current density accelerates the electrochemical reaction inside the porous electrode. At the initial stage of the reaction, the OH^- in the area far from the near flow channel side is rapidly consumed, and OH^- near the runner side has not yet been replenished. Thus, the average OH^- concentration on the near and far flow channel sides is rapidly reduced. Thus, the area inside the porous electrode away from the near flow channel side has a large concentration gradient. Driven by this concentration gradient, the diffusion coefficient is increased. The OH^- near the flow channel can enter the porous electrode quickly as a supplement. Therefore, the OH^- concentration decreases rapidly and then increases slowly.

Table 2 below shows that as the charging current density increases, the maximum value of the OH^- average concentration difference between the near and far runner sides and the time step required.

Table 2. Maximum value of the average OH^- concentration difference between the near and far runner sides with different charging current densities and the required time step

condition	Charging current density	Peak value of OH^- concentration difference between the near and far runner side（mol/L）	Time step
Electrode thickness 400μm Porosity 0.45	$6\text{mA}/cm^2$	0.3065	7×10^5
	$9\text{mA}/cm^2$	0.3884	6×10^5
	$12\text{mA}/cm^2$	0.4471	5×10^5
	$15\text{mA}/cm^2$	0.4936	4.5×10^5
	$18\text{mA}/cm^2$	0.5315	4×10^5

Table 2 shows that, as the current density increases, the time step required for the average OH^- concentration difference to a maximum decreases. The larger the current density, the larger the peak value. Therefore, excessive may cause concentration polarization. A large concentration gradient in the area far from the side near the flow channel, exists, which increases the diffusion coefficient of OH^-, and accelerates the diffusion rate of OH^- . This occurrence shortens charging time to a certain extent.

3.3 Effect of positive electrode thickness

In considering the effect of the electrode thickness, the charging current density was taken as $12\text{mA}/cm^2$, and the porosity is 0.45. Figs .7(a), (b), and (c) show that under the five electrode thickness

of 200μm、250μm、300μm、350μm、400μm, changes in the average OH^- concentration in the direction of the runner and its difference between the near and far runner sides in the area of porous media with the charging time step.

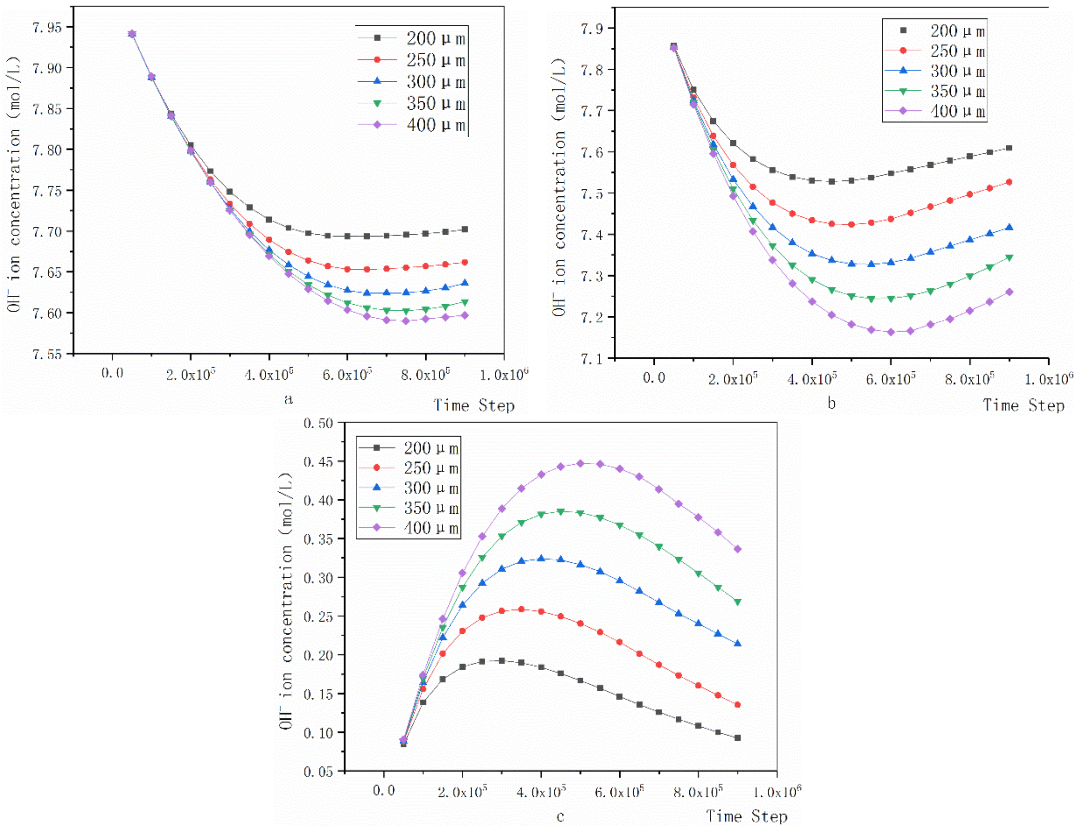

Figure 7. OH^- average concentration, (a) Near runner side, (b) Far runner side, and (c) Difference of OH^- concentration in near and far runners

Figure 7 shows that the average OH^- concentration near the flow channel decreases rapidly and then stabilizes and rises. However, the increase is small and the change trend of different electrode thicknesses is basically the same. The thicker the electrode, the later the electrode rises. On the far runner side, compared with the near runner side, the average concentration of OH^- decreases significantly with the increase of electrode thickness in the initial stage of charging.A significant difference exists between different electrode thicknesses. As the charging time progresses, the average OH^- concentration gradually rises. The larger the electrode thickness is, the later the rise time is, but the rise value is relatively large. The OH^- average concentration difference increases rapidly and then begins to decrease slowly. The larger the electrode thickness, the larger the OH^- average concentration difference.The faster the electrode rises and falls, the later the electrode reaches the maximum value.

For a zinc-nickel single flow battery, the change in the average OH^- concentration on the near and far side of the flow channel is mainly affected by the OH^- consumption and diffusion rate in different regions in the electrode thickness direction. On the near flow channel side, because of the influence of convection diffusion in the mainstream region, the change in the average OH^- concentration is smaller. As the electrode thickness increases, the internal diffusion resistance of OH^- increases. Thus,

the larger the electrode thickness, the smaller the change in the average OH^- concentration in the initial reaction. However, as the reaction progresses, a larger electrode thickness consumes more OH^-, making the average OH^- concentration decrease more.Moreover, the later the average OH^- concentration rises. On the far runner side, in the initial stage of the reaction, the decrease in the average OH^- concentration is mainly because of the local OH^- participating in the reaction consumption. However, as the reaction progresses, the OH^-diffuses from the side of the near-runner to the side of the far-runner, constantly replenishing the OH^- consumed by the reaction, and the protons in some particles on the side of the remote channel have been consumed. The decline in the average OH^- concentration on the side of the remote channel has gradually stabilized and picked up. Compared with the near-flow channel side, which is less affected by convection diffusion in the mainstream region, the average OH^- concentration change is significantly larger than that of the near-flow channel side.

Therefore, the increase in electrode thickness increases the diffusion resistance of OH^- in the thickness direction of the porous electrode, and reduce the diffusion coefficient of OH^-, thereby reducing the diffusion rate of OH^- and the charging efficiency of the battery.

Table 3 shows that, as the charging time step goes, the maximum value of the OH^- average concentration difference between the near and far runner sides and the time step required.

Table 3. Maximum value of the average OH^- concentration difference between the near and far runner sides with different electrode thickness and the required time step

condition	Electrode thickness	Peak value of OH^- concentration difference between the near and far runner side （mol/L）	Time step
Porosity 0.45 Charging current density $12\text{mA}/cm^2$	200μm	0.1925	3.0×10^5
	250μm	0.2585	3.5×10^5
	300μm	0.3239	4.0×10^5
	350μm	0.385	4.5×10^5
	400μm	0.447	5.0×10^5

Table shows that, as the electrode thickness increases, the peak value of the OH^- concentration difference gradually increases, and the charging time step required to reach the maximum value of the concentration difference increases. Thus, an increase in electrode thickness results in an increase in cell concentration polarization.

3.4 Effect of porosity

In considering the effect of the porosity, electrode thickness was taken as 400 μm, and the charging current density was$12mA/cm^2$. Figs. 8(a), (b), and (c) show the changes of the three porosities of 0.35、0.45、0.55, in the average OH^- concentration in the direction of the runner and their differences between the near and far runner sides in the area of porous media with the charging time step.

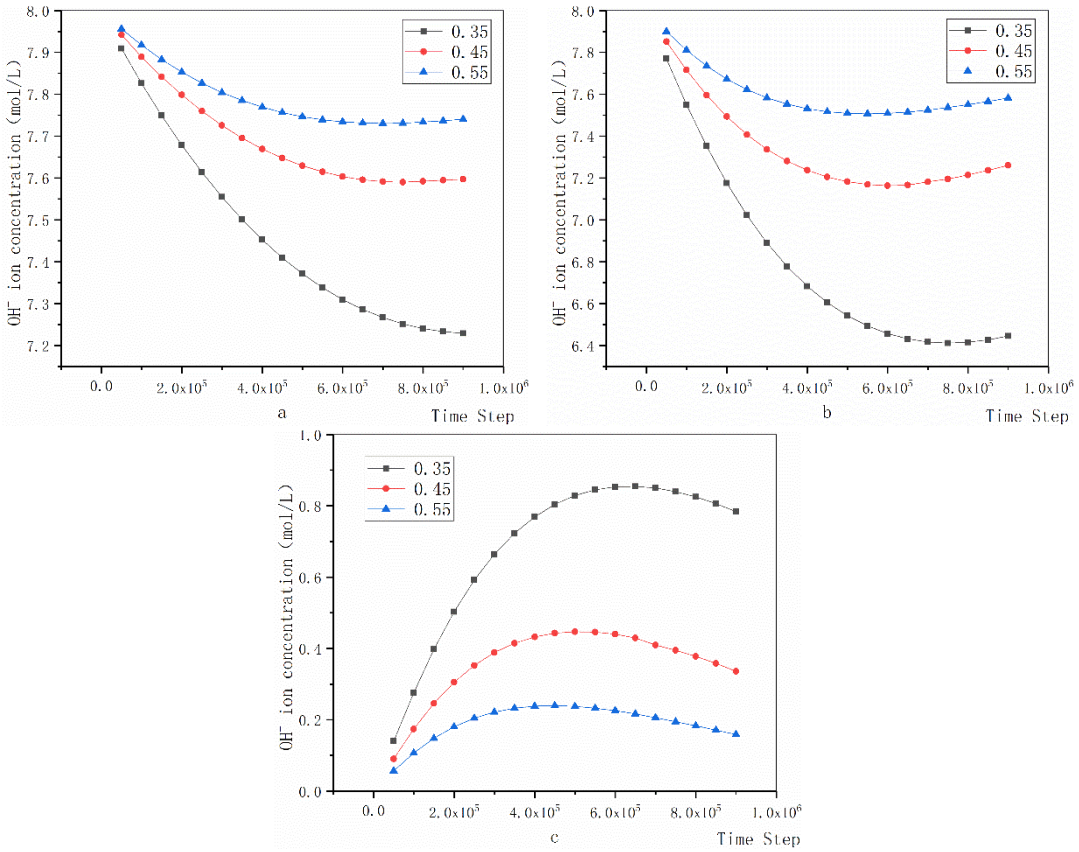

Figure 8. OH^- average concentration, (a) Near runner side, (b) Far runner side, (c) Difference of OH^- concentration in near and far runners

Figure 8 shows that the average OH^- concentration on the near and far runner sides decreases rapidly and then the decline rate slows. Thereafter, the rate picks up. The decrease in the OH^- concentration on the far runner side is larger than that on the near runner side, which rises earlier. A comparison of the different porosities show that the larger the porosity, the later the OH^- concentration rises, and the greater the decline and recovery.

When the charging step is 600,000 steps, the whole field cloud diagram of OH^- concentration and the change of OH^- concentration inside a given observation area with different porosities are shown in Figure 10.

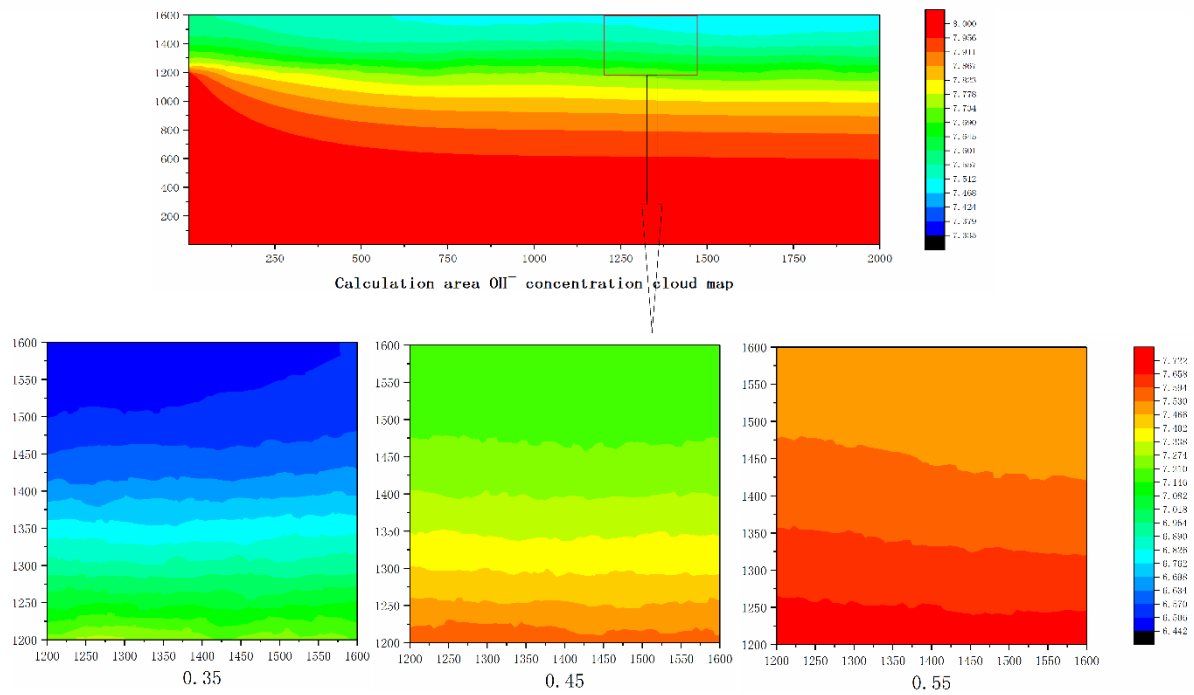

Figure 9. Variation of OH^- concentration in porous media under different porosities

Figure 9 shows that the smaller the porosity, the lower the overall OH^- concentration in the porous medium region. Under three different porosities, the change of OH^- concentration near the flow channel side is not apparent. However, the far flow channel side is very noticeable.

Comparing the analysis of the effect of electrode thickness on OH^- concentration and combining with Fig. 8, a conclusion that the change in OH^- concentration is mainly affected by the reaction consumption rate and diffusion rate in different regions in the electrode thickness direction can be made. When the porosity is small, few channels for OH^- transport exist inside the porous electrode. Thereafter, the diffusion resistance increases. The increase in porosity can reduce the diffusion resistance of OH^- in the porous medium. Thus, the OH^- near the flow channel can diffuse into the porous medium to react fast, thereby improving the charging efficiency of flow batteries.

Table 3 shows that as the charging time step goes, the maximum value of the OH^- average concentration difference between the near and far runner sides and the time step required.

Table 3. Maximum value of the average OH^- concentration difference between the near and far runner sides with different porosity and the required time step

condition	Porosity	Peak value of OH^-concentration difference between the near and far runner side（mol/L）	Time step
Electrode thickness 400μm Charging current density12mA/ cm^2	0.35	0.85450	6.5×10^5
	0.45	0.44704	5.0×10^5
	0.55	0.23964	4.5×10^5

Table 3 shows that as the porosity increases, the charging time step required for the OH^- concentration at the near and far runner sides to reach the maximum decreases. The smaller the porosity, the larger the peak value of the concentration difference. The above data shows that a very small porosity may lead to large concentration polarization.

The charging efficiency of a zinc-nickel single-flow battery mainly depends on the diffusion rate of OH^- inside the electrode. The above analysis shows that the above three factors all affect the diffusion rate by changing the diffusion resistance and diffusion coefficient of OH^-, thereby changing the average concentration. Further comparison and analysis of Tables 2, 3, and 4 shows that the effect of changing electrode thickness on the OH^- diffusion rate is the largest, and has the greatest effect on the concentration polarization and charging efficiency.

4. CONCLUSION

In this study, for the zinc-nickel single flow battery, a REV-scale transient mass transfer and chemical reaction model is established. Numerical simulation is performed using LBM. The effects of charging current density, electrode thickness, and porosity on the internal mass transfer and electrochemical reaction of zinc–nickel single-flow batteries were investigated during the transient process. The following conclusions were reached:

（1） Increasing the current density can reduce the charging time, but the effect of reducing the charging time becomes gradually small as the current density increases. Excessive current density may cause excessive concentration polarization in the electrode thickness direction.

（2） The larger the electrode thickness, the smaller the overall OH^- concentration inside the porous motor. Excessive electrode thickness causes high concentration polarization.

（3） When the porosity is small, the diffusion resistance of OH^- increases, which increases concentration polarization. When the resistance of OH^- transmission increases, the electrochemical reaction inside the electrode becomes adversely affected.

（4） A comparison of three factors shows that the electrode thickness has the greatest influence on the electrochemical reaction mechanism.

References

1. S. Ould Amrouche,D. Rekioua,T. Rekioua and S. Bacha. *Int.J. Hydrogen Energy*, 41(2016)45.
2. I. Hadjipaschalis,A. Poullikkas and V. Efthimiou. *Renewable Sustainable Energy Rev.*, 13(2008)6.
3. K.C. Divya and Jacob Østergaard. *Electr. Power Syst. Res.*, 79(2008)4.
4. J. Cheng,Y. Wen,G. Cao and Y. Yang. *J. Power Sources*, 196(2010)3.
5. J. Cheng,L. Zhang,Y. Yang,Y. Wen,G. Cao and X. Wang. *Electrochem. Commun.*, 9(2007)11.
6. B. Sharifi,M. Mojtahedi,M. Goodarzi and J. Vahdati Khaki. *Hydrometallurgy*, 99(2009)1.
7. J. Cheng,Y. Wen,G. Cao and Y. Yang. *J. Power Sources*, 196(2010)3.
8. Y. Cheng,H. Zhang,Q. Lai,X. Li,Q. Zheng,X. Xi and C. Ding. *J. Power Sources*,(2014)249.
9. J. Cheng,L. Zhang,Y. Yang,Y. Wen,G. Cao and X. Wang. *Electrochem. Commun.*, 9(2007)11.
10. Y. Ito,M. Nyce,R. Plivelich,M. Klein and S Banerjee. *J. Power Sources*, 196(2011)15.

11. Q. Liao,Y. Yang,X. Zhu and R. Chen. *Int.J. Hydrogen Energy*,38(2013)35.
12. H. Xu,Z. Dang and B. Bai. *J. Energy*,(2014),67.
13. J. Zhao, D. Fu,Y. Li, Y.Jiang,W.Xu and X.Chen. *J. Nat. Gas Sci. Eng.*, 57(2018)224.
14. L. Liu,J. Yao,L. Zhang,S. An,J. Zhao and H. Sun. *J. Nat. Gas Sci. Eng.*, 48(2017)100.
15. M. Xiao, Y. Wang, S. Yao, Y.Song and J.Chen. *J. Renewable Sustainable Energy*, 8(2016)6.
16. S. Yao, Y. Zhao, X. Sun, Q.Zhao and J.Chen. *Electrochim. Acta*, 307(2019)573.
17. S. Yao, Y. Li, L. Xu and J.Chen. *Energy Procedia*, 158(2019)4998.
18. S. Yao, L. Xu, Z. Sun and J,Chen. *Int. J. Heat Mass Transfer*, 138(2019)903.
19. S. Yao,H. Wu, M. Xiao, J.Chen and Y.Shen. *Int. J. Electrochem. Sci.*, 14(2019)8340.
20. P. Blaine, J. Newman, *J. Electrochem. Soc.*, 144(1997) 3818.
21. S P. Sullivan, F M. Sani and M L. Johns. *Chem. Eng. Sci.*, 60(2005)3405.
22. Q. Kang, Peter C. Lichtner and D. Zhang. *Water Resour. Res.*, 43(2007)W12S14.
23. H.Xu, Z.Dang and B,Bai. *J. Fuel Cell Sci. Technol.*, 9(2012).